Sheffield Hallam University

The role of forebody topology on aerodynamics and aeroacoustics characteristics of squareback vehicles using Computational Aeroacoustics (CAA)

VISWANATHAN, Harish and CHODE, Kushal Kumar

Citation:

Copyright and re-use policy

Check for
updates

The Role of Forebody Topology on Aerodynamics and Aeroacoustics Characteristics of Squareback Vehicles using Computational Aeroacoustics (CAA)

Harish Viswanathan[1,2] · Kushal Kumar Chode[1]

Abstract

This study investigates the influence of forebody configuration on aerodynamic noise generation and radiation in standard squareback vehicles, employing a hybrid computational aeroacoustics approach. Initially, a widely used standard squareback body is employed to establish grid-independent solutions and validate the applied methodology against previously published experimental data. Six distinct configurations are examined, consisting of three bodies with A-pillars and three without A-pillars. Throughout these configurations, the reference area, length, and height remain consistent, while systematic alterations to the forebody are implemented. The findings reveal that changes in the forebody design exert a substantial influence on both the overall aerodynamics and aeroacoustics performance of the vehicle. Notably, bodies without A-pillars exhibit a significant reduction in downforce compared to their A-pillar counterparts. For all configurations, the flow characteristics around the side-view mirror and the side window exhibit an asymmetrical horseshoe vortex with high-intensity pressure fluctuations, primarily within the confines of this vortex and the mirror wake. Side windows on bodies with A-pillars experience more pronounced pressure fluctuations, rendering these configurations distinctly impactful in terms of radiated noise. However, despite forebody-induced variations in pressure fluctuations impacting the side window and side-view mirror, the fundamental structure of the radiated noise remains relatively consistent. The noise pattern transitions from a cardioid-like shape to a monopole-like pattern as the probing distance from the vehicle increases.

List of Symbols

x, y, z	3D Cartesian coordinates (Streamwise, normal, spanwise)
L	Length of the vehicle

✉ Harish Viswanathan
h.viswanathan@shu.ac.uk

1 Materials and Engineering Research Institute, Sheffield Hallam University, Howard Street, Sheffield S1 1WB, England, UK

2 Department of Engineering and Mathematics, Sheffield Hallam University, Howard Street, Sheffield S1 1WB, England, UK

W	Width of the vehicle
H	Height of the vehicle
l_c	The characteristic length of the mirror
g_c	Ground clearence
ϕ	Diameter of the stilts
U_∞	Freestream velocity
p	Fluid pressure
p_∞	Operating pressure
δ_{99}	Boundary layer thickness
$\Delta x^+, \Delta y^+, \Delta z^+$	Dimensionless wall units
f	Frequency
ρ	Fluid density
Re_L	Reynolds number based on length of the vehicle
Re_H	Reynolds number based on height of the vehicle
F_s, F_d, F_l	Force components
$Cd_{vehicle}$	Drag coefficient of the whole vehicle
$Cl_{vehicle}$	Lift coefficient of the whole vehicle
Cd_{svm}	Drag coefficient of the mirror
Cd_m	Pressure drag of the mirror
Cd_b	Base pressure drag
Cd_f	Front slant pressure drag
Cd_{wm}	Pressure drag extracted on the mirror side
$Cd_{w'm}$	Pressure drag extracted on the no mirror side
Cp	Pressure coefficient
p'	Pressure fluctuations
St	Strouhal number
A	Reference area of the vehicle including the mirror and struts
S	Reference area of the mirror
V_1, V_2	Mirror induced vortices
V_r	Roof leading edge vortex
α, α'	Angle made by the vortices w.r.t central axis of the mirror
w_m	Mirror side of the vehicle
w'_m	No mirror side of the vehicle
L_{hx}	The thickness of the horseshoe vortex
L_{hy+}	Width of the horseshoe vortex in the positive normal direction
L_{hy-}	Width of the horseshoe vortex in the negative normal direction
L_{hz}	Width of the horseshoe vortex in the normal direction
L_{ws}	Length of the mirror wake
p'_{rms}	Root mean square of hydrodynamic pressure fluctuations
p'_n	Sound pressure fluctuations obtained at the far-field microphone location
p_{nrms}'	Root mean square of the sound pressure fluctuations obtained at the far-field microphone location
f_{mc}	Mesh cut-off frequency
C	Speed of sound
Δ_c	Local size of the grid
λ_T	Taylor microscale
f_u, f_d	Upper and lower focus points

Abbreviations

AB	Ahmed body
CAA	Computational aeroacoustics
DDES	Delayed DES
DES	Detached Eddy simulation
FB	Fused generic-Ahmed body
FW-H	Ffowcs-Williams and Hawkings
GB	Generic bluff body
HB	Hybrid body
HPF	Hydrodynamic pressure fluctuations
IDDES	Improved DDES
LES	Large Eddy simulations
OASPL	Overall sound pressure level
PPW	Points per wave
RANS	Reynolds-averaged Navier stokes
RMS	Root mean square
SB	SAE-T4 body
SBES	Stress-blended Eddy simulation
SPL	Sound pressure level
SST	Shear stress transport
WB	Windsor body

1 Introduction

The automotive industry is continuously striving to revolutionise the aerodynamics and aeroacoustics environment of vehicles, aimed at alleviating discomfort, enhancing communication systems, reducing vehicular emission noise (such as the pass-by noise signature), influencing sound barriers on urban roads, and improving overall safety (Braun et al. 2013; Oettle and Sims-Williams 2017; Read and Viswanathan 2020; Wang et al. 2023). The sources of vehicle noise can primarily be classified into four categories: aerodynamic noise, ancillary system noise, and tire-road noise, with occasional secondary classifications such as slosh noise, which may gain prominence (Helfer 2005; Ganuga et al. 2014; Jadon et al. 2014). In the current era of vehicle electrification, aerodynamic noise is of primary significance during cruising, as wind-induced noise increases with vehicle speed and supersedes tire noise at approximately 100 km/h (Helfer 2005). The reduction of aerodynamic drag is a crucial objective for Electric Vehicle (EV) manufacturers, as it directly influences the driving range of electric vehicles. However, it is important to note that the significance of aerodynamics extends beyond mere energy efficiency. In the context of EVs, aeroacoustics also plays a critical role in enhancing the overall driving experience and passenger comfort. For example, eliminating exterior mirrors and replacing them with cameras and screens can further reduce wind noise and aerodynamic drag by up to 7%, regulatory obstacles currently hinder this approach, despite potential benefits for EV manufacturers (Goetchius 2011). Whilst reducing aerodynamic drag is crucial for EVs, it does not automatically ensure low wind noise. The primary factors causing aerodynamic drag and noise in a bluff body vehicle are attributed to flow separation around features such as A-pillar, exterior mirrors, and front side glass, which can lead to wind noise issues independent of drag. It is important to highlight that these features are situated in the forebody of

the vehicle, where the interaction with the upstream flow can give rise to distinctive pressure fluctuations and radiated noise in addition to the aerodynamic forces experienced by the vehicle. For instance, the interface between the A-pillar and mirror generates much of the high-frequency aeroacoustics energy radiated from the vehicle (Chode et al. 2023; He et al. 2020; Dawi and Akkermans 2019) in addition to altering the vehicle drag by ~13.3% (Chode et al. 2023). Therefore, alongside the emphasis on aerodynamic drag reduction, there is a growing recognition of the importance of addressing the overall aeroacoustics signature of the vehicle (Camussi and Bennett 2020; Ask and Davidson 2010; Hamiga and Ciesielka 2020; Nusser and Becker 2021; Viswanathan and Chode 2023).

Many studies have employed a range of experimental and numerical techniques to examine the mechanisms underlying wind-induced noise radiation. These studies have covered a wide spectrum of scenarios, ranging from isolated features such as generic half-round side-view mirrors (Ask and Davidson 2009; Chode et al. 2021; Frank and Munz 2016a; Egorov et al. 2010; Wagner et al. 2007) to standard squareback SAE-T4 geometries that incorporate simplified side-view mirror representations with both generic and modified A-pillars (Dawi and Akkermans 2019; Hartmann et al. 2012; Nusser 2019). Investigations have also been conducted on SAE-T4 models without side-view mirrors but with an A-pillar (Chode et al. 2023; Müller et al. 2013), as well as with realistic mirrors (Hartmann et al. 2012; Kapellos et al. 2019; Evans et al. 2019). These investigations have shed light on the interactions between separated flows resulting from different A-pillar topologies, thereby altering the mirror wake vortices and pressure recovery and subsequently enhancing the generation and propagation of noise radiated from vehicles.

Numerical approaches for aeroacoustics simulations can be broadly categorized as hybrid and direct methods. Hybrid methods commonly employ incompressible Computational Fluid Dynamics (CFD) coupled with aeroacoustics analogy techniques, such as Möhring, Ffowcs Williams–Hawkings (FW-H), and Kirchhoff aeroacoustics equations (Hartmann et al. 2012). The hybrid approach effectively decouples the flow and acoustic solvers, resulting in a less computationally demanding solution. While both hybrid and direct methods play pivotal roles in understanding the pressure fluctuations and flow characteristics around automotive components, they are applied differently based on specific objectives. Direct methods, which involve computationally demanding compressible CFD, are employed to capture induced convective and acoustic pressure fluctuations, often utilising wavenumber filtering techniques. These methods have proven valuable in analysing near-field flow around features such as side windows, mirrors, and A-pillars. For instance, studies by Frank and Munz (2016b), Dawi and Akkerman (2018), Beck and Munz (2018), and Job and Sesterhenn et al. (2016) have successfully utilised direct methods to identify tonal noise generation mechanisms on realistic side view mirrors.

On the other hand, hybrid methods are widely used for studying noise characteristics in the far field, particularly focusing on the noise radiating away from the vehicle at much lower computational cost compared to Direct methods. Some of the works using hybrid method include Chode et al. (2023) where they reported that the radiated pattern shows a transition from dipole-like structure to monopole-like when measuring distance is traversed away from the vehicle. While He et al. (2021b) demonstrated the capability of hybrid method for obtaining interior noise levels and observed that the contribution of acoustic pressure fluctuations is dominant at frequencies ranges above coincidence frequency of the glass.

The distinct strengths of direct methods lie in comprehending noise transmission mechanisms to the vehicle's interior. Thus, the combined use of both hybrid and direct methods offers a comprehensive approach to gaining valuable insights into the intricate

dynamics of automotive aerodynamics, providing a holistic understanding of both the near-field and the far-field noise signatures (Dawi and Akkermans 2019). In the realm of computational aerodynamics and aeroacoustics for automotive vehicles, RANS-LES methods have emerged as prominent approaches over the past two decades. Regardless of the chosen approach for investigating both vehicle aerodynamic performance and aeroacoustics (direct or hybrid), RANS-LES methods have gained recognition for their ability to deliver solutions with superior accuracy compared to the RANS approach (Hamiga and Ciesielka 2020; Viswanathan 2021; Höld et al. 1999) while remaining computationally more efficient than the full LES subjected to realistic flow conditions (Chode et al. 2023, 2020; Menter et al. 2021; Nusser et al. 2017). To date, various RANS-LES variants, viz., DES, DDES, IDDES, and SBES approaches coupled with near-wall modelling using SST, SA, and k-ε approaches, have been extensively applied to generic and non-generic mirror geometries (Frank and Munz 2016b; Dawi and Akkermans 2018; Beck and Munz 2018; Job and Sesterhenn 2016), SAE-T4 and DrivAer vehicle configurations (He et al. 2020, 2021a; Dawi and Akkermans 2019; Hartmann et al. 2012). RANS-LES-based numerical investigations on these geometries have not only shown excellent agreement with experiments but have also enhanced our understanding of flow physics. In particular, comparisons under different fluid assumptions (compressible or incompressible) revealed insignificant differences in all frequency bands for hydrodynamic pressure fluctuations on the side window (Dawi and Akkermans 2019; Hartmann et al. 2012; He et al. 2021a). The IDDES and the SBES-based predictions on the SAE-T4 (Chode et al. 2023; Dawi and Akkermans 2019; Menter et al. 2023) body have particularly revealed several insights, including (i) the A-pillar serves as the primary noise source in the absence of a side mirror, while in the presence of a side-view mirror shifting the focus to the mirror as the major noise source; (ii) the turbulent pressure fluctuations predominantly excite the window below 800 Hz, while acoustic pressure fluctuations dominate above 800 Hz; (iii) for frequencies lower than 1 kHz, hydrodynamic pressure fluctuations are primarily responsible for the window excitation; and (iv) the noise radiated from the vehicle can exhibit dipole-monopole transitions at several stages based on the noise source in consideration. Despite such considerable efforts invested, several questions and unresolved aspects persist.

To the best of the authors' knowledge, existing studies on vehicle aeroacoustics have predominantly centred around SAE-T4 and DrivAer configurations, both featuring distinct A-pillars. However, there is a noticeable gap in utilising the hybridized RANS-LES approaches coupled with far-field approaches such as the Ffowcs Williams-Hawkings (FW-H) to predict noise signatures from various standardized vehicle configurations. Additionally, the intricate vortex structures produced by standard bluff mirrors remain unexplored, prompting questions about potential alterations influenced by different standard forebodies and their subsequent influence on the overall base wake of the vehicle. The relationship between aerodynamic forces experienced by diverse forebody configurations of squareback bodies and their potential influence on radiated sound is of notable interest but has received relatively limited exploration. These unexplored aspects represent a substantial knowledge gap in the current understanding of vehicle aeroacoustics and aerodynamics of different forebody squareback vehicles. The present work is primarily motivated by these critical gaps, aiming to bridge the gap in the literature by providing insights into the FW-H approach's application, the nature of vortex structures in standardized bluff mirrors, and the intricate interplay between aerodynamic forces and radiated sound across different squareback body configurations.

The current study employs the SBES modelling approach coupled with the FW-H acoustic equation to describe the near-field flow and far-field noise, respectively. The key

aims of the current study are threefold: (i) to investigate the pattern of noise generated and radiated in six squareback vehicle configurations, identifying influential forebody designs, (ii) to examine the role of A-pillars in modifying/interacting with the vortices generated by mirrors and their effects on noise, and (iii) to explore the relationship between hydrodynamic pressure fluctuations on the side window, radiated noise, and corresponding aerodynamic coefficients associated with different forebody vehicle configurations.

This paper is organised as follows: Sect. 2 focuses on "System Details and Forebody Design Configurations", presenting the selection and details of the topologies of the forebody configurations used in the study. In Sect. 3, "Numerical and Computational Details," the computational domain, grid details, boundary conditions, grid independence, and validation of the SBES-FWH method are discussed. Section 4, "Results and Discussions", offers an intricate analysis of surface pressure spectra, flow fields, and the generated and radiated noise, providing an in-depth exploration of acoustic signatures within diverse forebody squareback configurations. Additionally, this section presents a comprehensive assessment of the aerodynamic coefficients and aerodynamics-aeroacoustics characteristics associated with the different forebody topologies employed. Finally, Sect. 5, "Conclusions" summarizes the crucial contributions and findings derived from the study.

2 System Details and Forebody Design Configurations

2.1 Forebody Topologies

In this work, the study comprises two distinct categories of full-scale simple squareback representations: bodies without a distinctive A-pillar and bodies with such a characteristic, thereby addressing the fundamental objectives outlined previously. Regarding the former, this study considers the Generic Bluff Body (GB), a model proposed by Duell and George (1999), which has been utilised with LES by Krajnović and Davidson (2003), as well as the Ahmed body (AB) (Ahmed et al. 1984). As the primary focus of this research is the examination of the influence of forebody topology, a novel amalgamation of GB and AB, termed the Fused Generic-Ahmed Body (FB), is devised. Within the FB configuration, the upper portion of the forebody is meticulously designed to mirror the dimensions of the Ahmed body's radii, whereas the lower portion retains an identical profile to that of the GB's. The primary motivation behind this configuration change is to investigate the consequences of leading-edge separation bubbles that form around the different curvatures of forebody corners, the periodic interaction of the upper and lower partitions of the ring vortex in the near wake of the body (contributing to drag), and the resulting near- and far-field noise signatures.

The latter category includes well-studied forebody topologies, such as the SAE T4 body (SB) (Chode et al. 2023; Nusser 2019; Müller et al. 2013), extensively investigated for Aeroacoustics, and the Windsor body (WB) (Windsor 1991; Perry et al. 2016a, 2016b), which has recently gained attention as a test case geometry, particularly with broader research participation aimed at comprehending various numerical modelling approaches (Page and Walle 2022). Both SB and WB exhibited clearly defined but slightly exaggerated A-pillars, as shown in Fig. 1. Modern square-back vehicles, such as but not restricted to the Mercedes T-Class and Citroën ë-Berlingo, inherit forebody features from the AB, SB, and WB, resulting in a detailed A-pillar structure arising from forebody curvature. To address this configuration more closely and effectively understand the aerodynamics and aeroacoustics
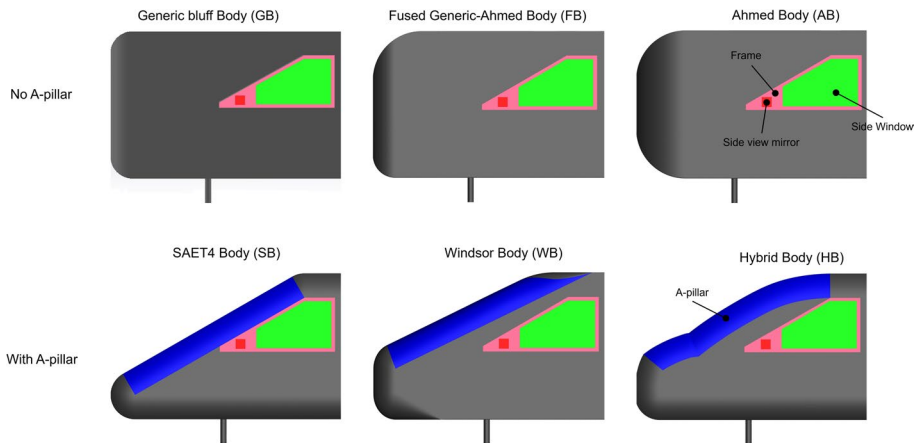
Fig. 1 Squareback geometries with distinct forebody configurations are used in this study. The figure illustrates the locations of key entities, including the side-view mirror, frame, and side window, for two categories of vehicles: those without the A-pillar and those with the A-pillar

effects of vehicles with curved A-pillars while retaining the features of standard research bodies, the Hybrid Body (HB) is introduced in this study which combines key forebody features of the geometries mentioned above.

2.2 Noise Sources: Location and Considerations

Previous experimental investigations of aeroacoustics and aerodynamics on full-scale squareback SAE-T4 geometry have identified key contributors to the overall noise radiation from the vehicle (Chode et al. 2023; Nusser and Becker 2021; Nusser 2019; Müller et al. 2013). These entities include the side-view mirror, A-pillar, side window, and frame, all of which are present within the forebody of the vehicle, as illustrated in Fig. 2a.

To ensure robustness, the employed modelling methodology is extensively verified and validated against the available experimental results of Nusser (2019), specifically concerning the full-scale squareback SB geometry (detailed in Sect. 3). However, for other squareback geometries examined in this study, no corresponding experimental data or numerical results are available for comparison. Therefore, to ensure consistency and enable meaningful comparisons, a meticulous approach is adopted in this study to preserve identical design characteristics for specific entities across all geometries, that is, standardising the origin, height (H), length (L), and reference area of the vehicle including mirror and struts (A) to match the SB geometry is a crucial aspect of this work, as shown in Fig. 2a. The side view mirror (see Fig. 2b) is represented as a generic square cylinder of length (l_c) in all vehicle configurations and the side window with the frame and its position remains identical from the point of origin throughout. All models are mounted on four identical stilts (ϕ) and the same ground clearance (g_c) dimension is also maintained across all model configurations, as shown in Fig. 2a. This comprehensive standardisation ensures a fair and unbiased assessment, enabling us to isolate and investigate the distinctive aeroacoustics and aerodynamic characteristics associated with each vehicle configuration, while effectively comparing them. The hydrodynamic excitation path on the side window of each examined geometry was probed at 39 evenly spaced measuring positions in the simulations, as
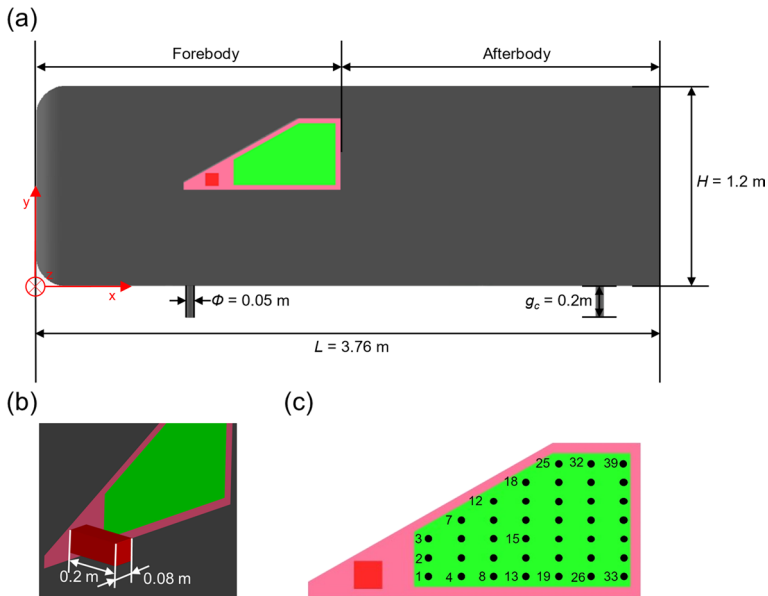
Fig. 2 **a** Illustrates the definition of the forebody and afterbody in one of the chosen vehicles, along with its dimensions and origin. The other five configurations in this study share identical characteristics with the forebody shape. **b** Depicts the generic square-cylinder mirror with its dimensions, which is consistent among all vehicle configurations. **c** represents the surface pressure probe locations on the side window, the same for all six studied geometries

depicted in Fig. 2c, emulating the approach used in the corresponding experiments (Nusser 2019; Müller et al. 2013). In the far-field, multiple locations were probed to capture a comprehensive representation of the noise radiated from various topologies, including those measured experimentally by Muller et al. (2013). For the convenience of readers, the complete set of CAD geometries, along with their dimensions and probing locations, are available for download from the Supplementary Material.

3 Numerical and Computational Details

The geometries studied are enclosed within a computational domain, aligned with dimensions specified in terms of vehicle length (L), width (W), and height (H), as shown in Fig. 3. The domain configuration is intentionally scaled up in overall size to be tailored for ground vehicle aeroacoustics, facilitating vehicle aeroacoustics simulations in strict accordance with the ERCOFTAC guidelines. This strategic adaptation is substantiated by the outcomes of previous numerical studies (Chode et al. 2023; Hartmann et al. 2012; Nusser 2019). The origin of the coordinate system, is located in the front of the geometry, as shown in Fig. 3. The inlet is located $3L$ from the origin, and the outlet is located at $9L$. The cross-section of the domain is set at $11.1\,H \times 8.32\,W$, which results in a blockage ratio of $\sim 1.5\%$, consistent with the previous setup (Chode et al. 2023).

For all cases, a uniform inflow velocity (U_∞) of 27.78 m/s is assigned to the inlet which corresponds to a Reynolds Number $Re_L = 7 \times 10^6$ based on the length of the body. The inlet
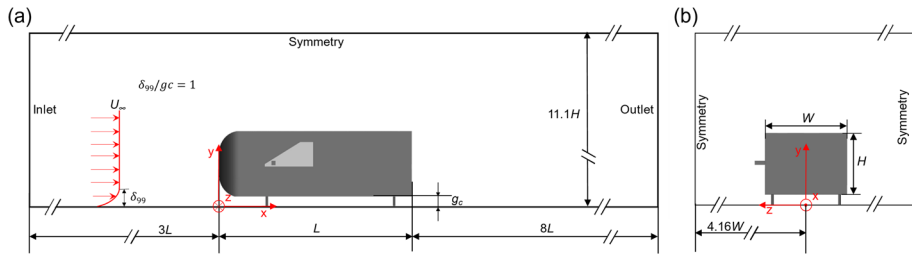
Fig. 3 Schematic of the computational domain used in this study, one representative body configuration applicable to all cases: a) side view and b) rear view

turbulent intensity is set to 0.1%, which is identical to the inflow conditions used in the experimental studies conducted by Müller et al. (2013) and Nusser (2019). The ratio of the 99% boundary layer thickness (δ_{99}) and ground clearance (g_c) is set to 1, which ensures that the effect of the ground boundary layer on the vehicle flow characteristics is minimal (Su et al. 2023). A zero pressure is defined for the outlet, and the surrounding walls are defined as symmetry as shown in Fig. 3. The no-slip condition is assigned to the ground and vehicle body.

The simulations conducted in this study were carried out using ANSYS Fluent 2020 R2. Considering that the inflow velocity, corresponding to a Mach number (M) less than 0.1, the effect of compressibility is negligible, therefore, the flow is treated as incompressible which is in consistent with previous studies (Chode et al. 2023, 2021; Hartmann et al. 2012; Nusser 2019; Ekman et al. 2019). A stress-blended Eddy Simulation (SBES) turbulence model was employed to capture the flow field around the vehicle body. SBES has shown promising accuracy in predicting flow characteristics and resolving flow structures compared with other widely used turbulence models (Chode et al. 2023, 2021; Ekman et al. 2019). The unique advantage of SBES is its ability to rapidly switch from RANS to LES modes in shear-separated layers and provide asymptotic shielding to RANS layers under heavy grid refinement (Menter 2018; Menter et al. 2021). Following the approach described in Chode et al. (2023), the same methodology and setup conditions were applied in this study. Regarding the numerical schemes, a bounded central difference scheme was employed for spatial discretisation and a bounded second-order implicit scheme was used for time advancement.

For unsteady SBES calculations, a fully converged solution obtained from the steady-state $k\text{-}w$ shear stress transport (SST) turbulence model was used as the initial solution. To achieve a statistically converged solution, a time step of 1×10^{-4} s was employed, and the simulations were conducted for a physical time of 0.3 s. Subsequently, the time step was reduced to 2.3×10^{-5} s, and the simulations were extended for an additional physical time of 0.35 s. To mitigate potential instabilities resulting from the timestep change, the initial 0.05 s is omitted from the time-averaging process. For further details on the numerical setup, readers are directed to the work of Chode et al. (Chode et al. 2023). For acoustic calculations, the surface pressure fluctuations exerted on the side window, side-view mirror, frame, and A-pillar are obtained through out the time-averaging period. Approximately 13,000 samples were collected and utilised as inputs for the FW-H acoustic analogy to predict far-field radiated noise. Microphone positions around the vehicle body were strategically chosen for investigation. Acoustic pressure data obtained at each probe position in time-domain were transformed into frequency domain using Fast Fourier Transform (FFT) after preprocessing the time input with windowing functions for enhanced accuracy.

3.1 Grid Assessment

An unstructured Poly-hex core grid generated using a built-in meshing tool in Fluent was utilised in this study, with a specific focus on the forebody of the vehicle geometry. To achieve an accurate resolution of the wide range of turbulence structures responsible for exerting pressure fluctuations on solid surfaces, local grid refinements were generated to obtain a uniform distribution of cells. The surface grid sizes were determined based on wall-normalised units, whereas the free-stream sizes were estimated using characteristic length scales. The Taylor microscale (λ_T) is used as the reference eddy size to determine the eddies which are influenced by viscosity. Taylor microscale is defined as $\lambda_T \sim 5.5 \mathrm{Re}_H^{-1/2} H$ where Re_H is the Reynolds number based on the height of the vehicle (Chode et al. 2020; Fares 2006; Guilmineau et al. 2018; Howard and Pourquie 2002; Hesse and Morgans 2023).

For the grid evaluation and validation of the methodology, an SAE reference body with a squareback configuration (SB, see Fig. 1) was selected. The choice is based on the availability of reproducible and comparable experimental data from the published works of Nusser (Nusser 2019). To conduct the grid evaluation study, three poly hex core grids (Coarse, Medium, and Fine) are generated for the SB geometry. In the generation of all three grids, careful attention has been given to maintaining a $\Delta y^+ < 1$ on the SAE T4 body. The surface grid sizes were set as follows: for the coarse grid, $\Delta x^+ = 140$–1200 and $\Delta z^+ = 140$–1200; for the medium grid, $\Delta x^+ = 70$–980 and $\Delta z^+ = 70$–980 are used and for the fine grid, $\Delta x^+ = 70$–600 and $\Delta z^+ = 70$–600. Significant refinements have been made to the grid in the regions surrounding the wake of the vehicle and forebody. In the wake, the cell size of the grid has been reduced from $4\lambda_T$ (coarse) to λ_T (fine) and for the forebody, the grid size has been varied from $2\lambda_T$ (coarse) to $0.5\lambda_T$ (fine). An overview of the medium grid generated around the reference geometry is shown in Fig. 4. The total cell count of the medium grid for the geometries used in this study is approximately 25.2×10^6.

Comparing the coarse and medium grids, the overall drag coefficient ($Cd_{vehicle}$) shows a difference of 6.5%, whereas the difference between the medium and fine grids is 0.1%. The drag coefficient of the mirror ($Cd_{svm} = \frac{(2*F_s)}{\rho * U_\infty^2 * S}$, where F_s is Force component in streamwise direction and S represents Reference area of the mirror) exhibits similar differences, with a 4.62% difference between the coarse and medium grids and yielding a mere 0.5% difference between the medium and fine grids. A comparison was made between the time-averaged streamwise velocity predictions for the vehicle and wake, as illustrated in Fig. 5. The qualitative differences between the medium and fine grids were minimal, but a considerable difference was observed in the velocity profiles predicted by the coarse grid in the wake. From a quantitative standpoint, the maximum differences in the three grids are observed at $y/H = 1.21$, here, the difference between the medium and coarse grid amounts to 3.78%, while the disparity between the medium and fine grid is 1.22% at $y/H = 1.31$.

In addition, a comparison of the mesh cutoff frequencies for the sensor located on the side window was conducted. The mesh cut-off frequency, denoted as f_{mc}, is defined as $f_{mc} = \sqrt{2\langle k \rangle / 3} / (2\Delta_c)$, where $\langle k \rangle$ is the time-averaged kinetic energy, and Δ_c represents the length of the cell (Wagner et al. 2007). Both the medium and fine grids included a local refinement closer to the side window of $0.5\lambda_T$. This refinement corresponds to approximately 22 points per wave ($PPW = C/(f_{max}.\Delta_c)$, where c is the speed of sound) for a frequency of ~ 4 kHz.
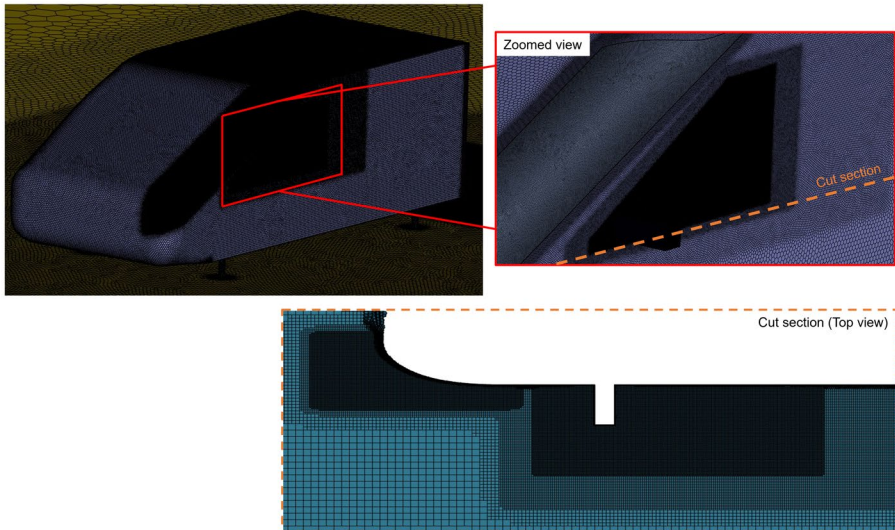
(a)
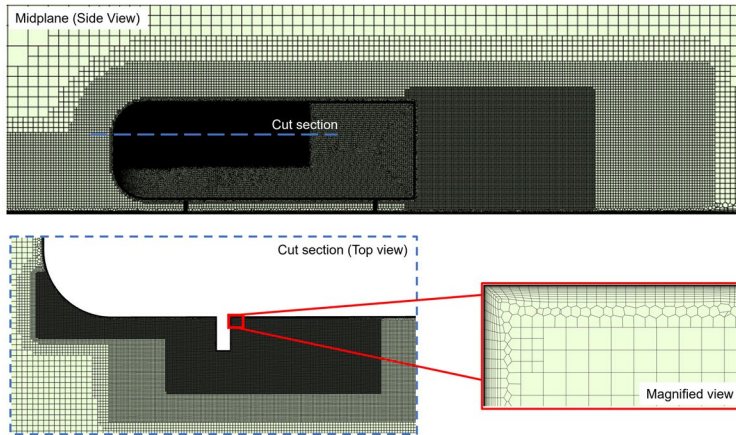
(b)

Fig. 4 **a** grid generated at the centre plane illustrating the distribution of local refinements around the Ahmed Body (AB) with a cut section illustrating the forebody refinements and a magnified view of the boundary layer; **b** illustrates the surface grid generated for the Windsor body (WB) with a zoomed view of the surface grid generated closer to the side window and a cut section illustrating the forebody refinements, including the A-pillar refinement

The mesh cutoff frequencies obtained for the five probe positions were compared and are presented in Table 1. The difference between the f_{mc} values obtained for both the fine and medium grids was less than 8 Hz on average. Interestingly, despite using smaller grid sizes in the fine-grid case, the difference between the fine and medium predictions was minimal.
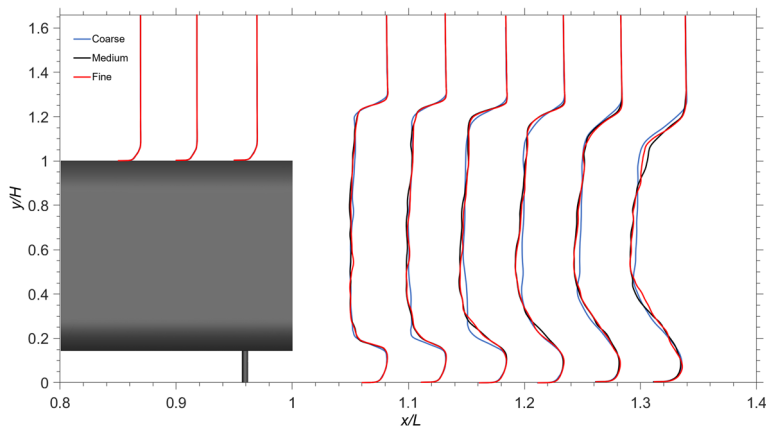
Fig. 5 Time-averaged streamwise velocity profiles over SB and in its wake for various grids used in this study

Table 1 Comparison of mesh cut-off frequencies for grids used in the study at various probe positions

Probe position	Coarse	Medium	Fine	%diff. (Coarse and Medium)	%diff. (Medium and Fine)
Pos 5	268 Hz	458 Hz	462 Hz	52.34	0.87
Pos 10	272 Hz	461 Hz	473 Hz	51.57	2.57
Pos 21	264 Hz	452 Hz	449 Hz	52.51	0.67
Pos 27	259 Hz	466 Hz	473 Hz	57.10	1.49
Pos 33	251 Hz	465 Hz	478 Hz	59.78	2.76

3.2 Validation and Verification

The methodology used in this study is validated using the experimental data presented by Nusser (2019). The pressure fluctuations obtained is processed using a sample frequency of 3 Hz with Hanning window and 50% overlap which is consistent with the methodology used in previous study (Chode et al. 2023, 2021). The hydrodynamic pressure fluctuations (HPF) obtained at Pos 1, situated on the side window (See Fig. 2c for identifying the sensor position on the side window), show that both the medium and fine grids predicted the presence of two aeolian tones at 40 and 80 Hz which agrees well with the experimental data (See Fig. 6). The peak observed in the experimental data and the predicted data correspond to a Strouhal number $\left(St = \frac{f.l_c}{U_\infty} \right)$ of 0.116, which corresponds to the St of the square cylinder at a Strouhal frequency of 40 Hz. Despite the accurate prediction of aeolian tones at peak frequencies corresponding to 40 and 80 Hz, a difference of 3.19 and 4.01% is observed in the amplitude predicted by the medium and 2.8 and 3.6% the fine grid respectively compared to the experimental data. Additionally, while the coarse grid configuration successfully predicts intensity levels comparable to those of the medium and fine grids, there are disparities of 6.6 and 4.4 Hz in the frequencies at which peak intensities are
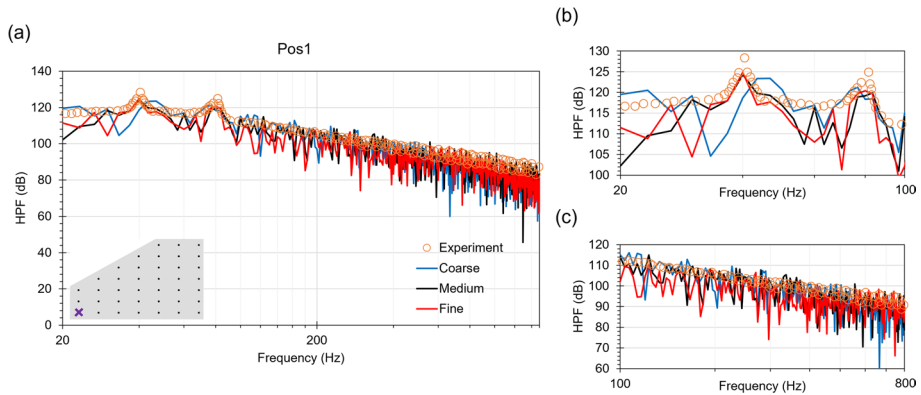
Fig. 6 Comparison of Hydrodynamic pressure fluctuations (HPF) at Pos 1 between the experiment and grids used in this study. **a** full-pressure spectra, **b** pressure spectra at low frequencies ($f < 100$ Hz), and **c** pressure spectra at medium frequencies (100 Hz $< f < 800$ Hz). The schematic within the plots represent the location where data was extracted

Table 2 Comparison of force coefficients and pressure drag coefficients of mirror (Cd_m), base (Cd_b), front slant (Cd_f), no mirror side ($Cdw_{,m}$) and mirror side (Cdw_m)

Model	Drag coefficient ($Cd_{Vehicle}$)	Lift coefficient ($Cl_{Vehicle}$)	Cd_m	Cd_b	Cd_f	Cdw_m	Cdw'_m	Difference ($Cd_{wm} - Cd_{w'm}$) (%)
GB	0.2601	−0.1768	0.9482	0.2049	0.3214	0.2305	0.2201	4.51
FB	0.2604	−0.1572	0.9501	0.2048	0.3521	0.2318	0.2213	4.53
AB	0.2598	−0.1774	0.9576	0.2039	0.3719	0.2393	0.2296	4.05
SB	0.2604	−0.1187	0.9753	0.2041	0.0731	0.1883	0.1711	9.13
WB	0.2573	−0.1383	0.9410	0.2017	0.1665	0.2096	0.1996	4.77
HB	0.2605	−0.1326	0.9772	0.2072	0.2358	0.2180	0.2068	5.14

projected, as compared to both the medium and fine grid configurations. Given the marginal differences observed between the medium and fine grids across a range of predictions, encompassing the pressure spectra, cut-off frequencies, HPF data, and velocity wake profiles, it becomes apparent that opting for the medium grid configuration is a notably prudent decision for this study. This choice is underpinned by its good agreement with the experimental results and reduced computational demand.

4 Results and Discussion

This section provides an in-depth analysis of the outcomes derived from numerical simulations, conducted on two fundamental aspects. Firstly, it delves into the prominent flow characteristics and aerodynamic forces arising from distinct forebody configurations. Subsequently, it explores the generation and emission of noise by these forebodies.
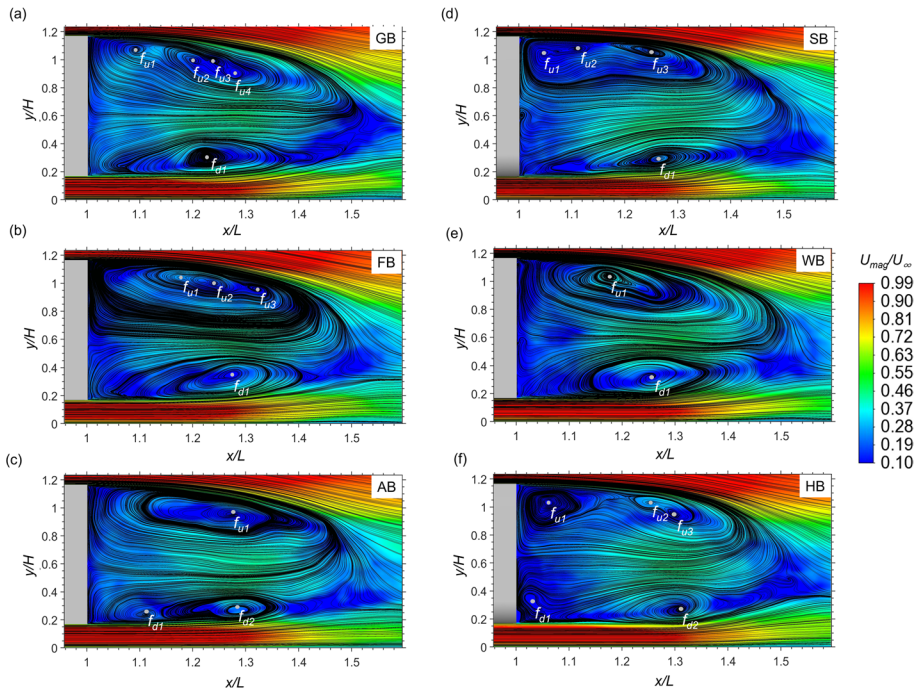
Fig. 7 Comparison of time-averaged quantities of the mean velocity generated at midplane ($z/W=0$) superimposed with the velocity streamlines in the wake between **a** GB, **b** FB, **c** AB, **d** SB, **e** WB, and **f** HB

4.1 Distinctive Flow Features of Various Forebody Squareback Configurations

The analysis of overall drag ($Cd_{vehicle}$ as defined in Eq. 1) across all configurations revealed a remarkable degree of uniformity, with variations of merely 1%, as presented in Table 2. Similarly, the predicted wake lengths for all cases as represented in Fig. 7 shows a high degree of similarity amongst all configurations examined in this study. In terms of lift characteristics, all configurations under scrutiny exhibited negative lift (downforce) obtained from $Cl_{vehicle}$ in Eq. (1). The (SB) configuration displayed the least downforce, while the (AB) design yielded the highest downforce. Notably, configurations featuring an A-pillar experienced significantly reduced downforce in comparison to their no A-pillar counterparts, emphasizing the influential role of the forebody in affecting the overall lift. This result was corroborated through the evaluation of forebody drag coefficient, denoted as Cd_f in Table 2 that elucidates that those configuration with A-pillars encountered lessened stagnation pressure on the front, in a marked contrast to those configurations without A-pillars examined in this study.

Furthermore, in Fig. 7 it is observed that all the bodies under examination exhibit a characteristic pattern of two distinct recirculation regions in their wake, upper and lower trapped vortices and the strength of the upper vortices is more compared to the lower vortices which is typical for a squareback configuration (Roumeas et al. 2009). The strength of the upper vortices increases with change in complex curvature of the forebody. In the case of bodies with A-pillars and rounded edges, namely the SB and HB, the focal point (denoted as f_u (upper) and f_d (lower)) f_{u1} appears closer to the base of the body. However, for the WB, which has a sharp
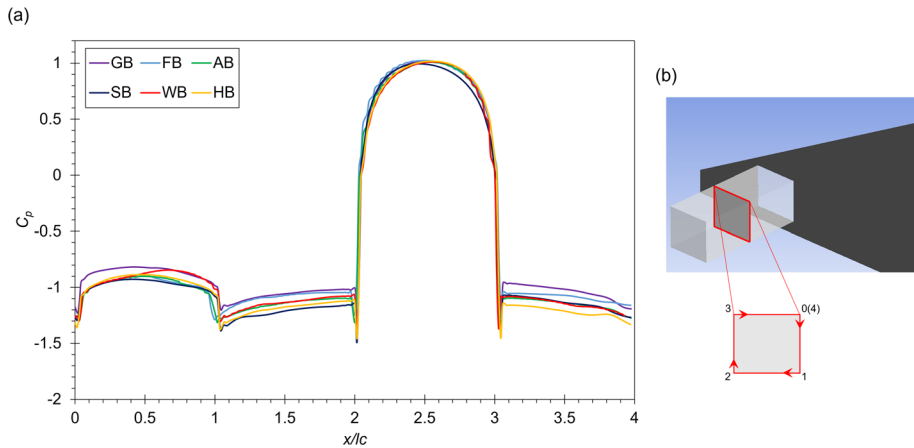
Fig. 8 a Comparison of coefficient of pressure (Cp) at the midplane of the side-view mirror between all models used in this study, **b** shows the location where Cp was extracted

edge at the base, the focal points diminish in number and appear further away from the base, indicating that the flow is less separated.

$$Cd_{vehicle} = \frac{2F_d}{\rho U_\infty^2 A}$$

$$Cl_{vehicle} = \frac{2F_l}{\rho U_\infty^2 A} \tag{1}$$

Here, $Cd_{vehicle}$, and $Cl_{vehicle}$ represent the coefficient of drag and lift respectively, while F_d and F_l indicate the predicted drag and lift force while A, is the reference area of the vehicle including the mirror and struts (Frontal Area).

$$Cp = \frac{p - p_\infty}{\frac{1}{2}\rho U_\infty} \tag{2}$$

where p_∞ and p are the static pressure in the freestream and at the point where the pressure coefficient is evaluated respectively and ρ is the density of the fluid in the freestream.

Figure 8 shows the pressure coefficient (Cp), defined as indicated in Eq. (2). The Cp profiles extracted from the midplane of the mirrors across all configurations reveal a consistent pattern that includes a stagnation point on the frontal surface peaking at $x/l_c = 2.5$, with flow separation occurring and not reattaching at the top and bottom surfaces of the mirror at $x/l_c = 1$–2 and 3–4. This behaviour is in line with previous studies on cubes and square cylinders, as demonstrated by Castro and Robbins (1977) and Wang et al. (2020). On the top surface of the mirror at $x/l_c = 3$–4, the Cp profiles for various forebody configurations exhibit similar curvatures, with the exception that mirrors mounted on bodies without A-pillar experience reduced flow separation compared to those with A-pillars. However, a notable observation lies in the $x/l_c = 0$–1 region, which corresponds to the rear side of the mirror. Here, it is intriguing to note that the GB and WB configurations demonstrate less flow separation compared to the other configurations, which is corroborated by the
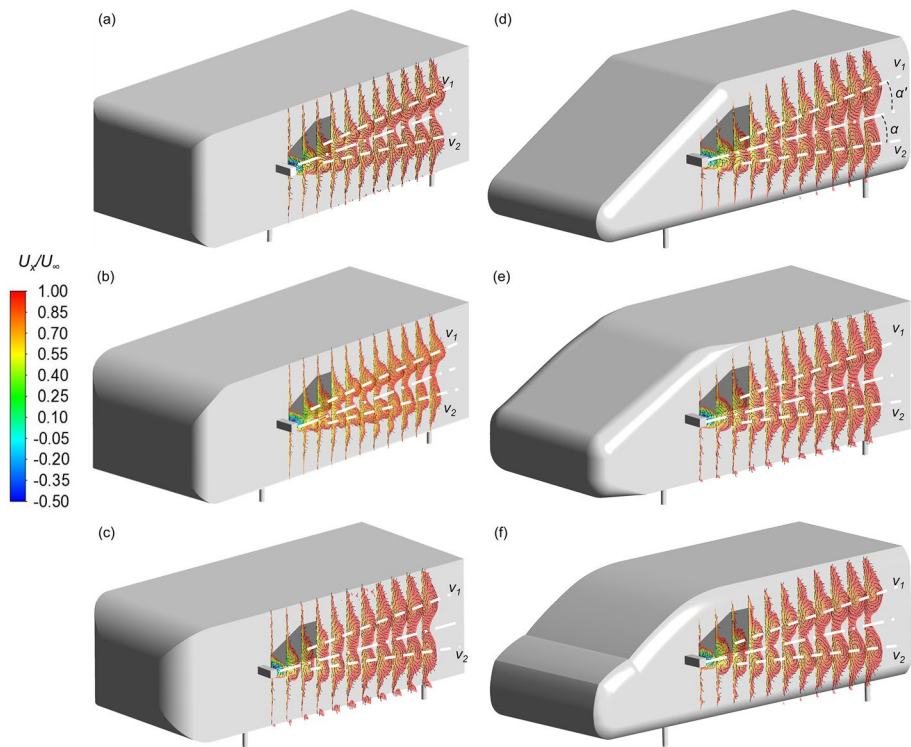
Fig. 9 Time-averaged normalised streamwise velocity plotted around the forebody of **a** GB, **b** FB, **c** AB, **d** SB, **e** WB, and **f** HB. Here, α', α represents the angle between the centre of the vortices and the horizontal axis of the mirror

Table 3 Comparison of mirror induced vortices and its strength for all the models used in the study

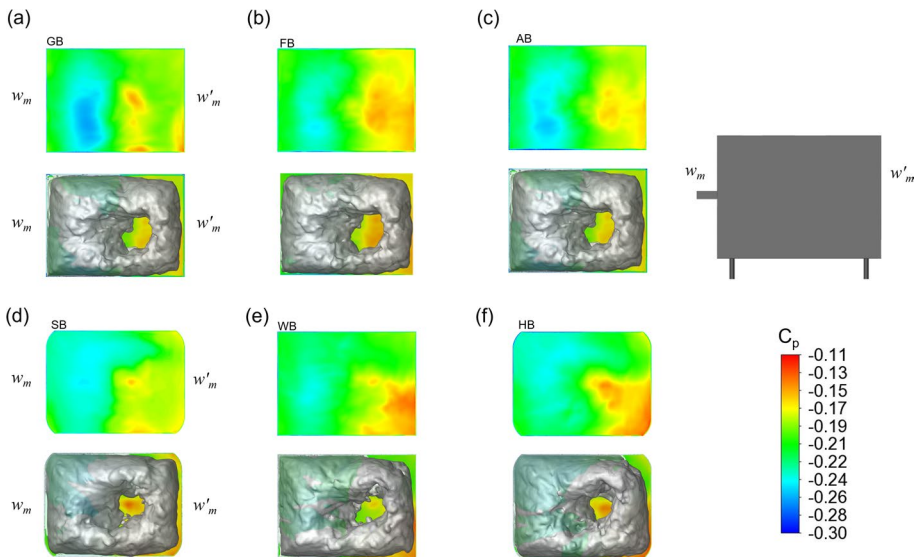| Model	α'	α		$x/L=0.48$	$x/L=0.53$	$x/L=0.59$	$x/L=0.64$
GB	5.27°	5.12°	V_1	23.78	24.36	24.76	24.88
			V_2	23.95	24.58	24.84	25.12
FB	5.26°	5.11°	V_1	22.48	23.08	23.65	23.98
			V_2	22.92	24.01	24.32	24.53
AB	5.28°	5.10°	V_1	22.64	23.11	23.45	23.79
			V_2	22.89	23.48	23.93	24.32
SB	6.60°	4.17°	V_1	23.05	23.85	24.30	24.65
			V_2	22.72	23.46	23.92	24.30
WB	4.92°	4.78°	V_1	23.72	24.19	24.36	24.52
			V_2	22.97	23.67	24.01	24.35
HB	5.32°	4.74°	V_1	23.49	23.99	24.39	24.67
			V_2	23.17	23.6	24.04	24.46

Fig. 10 Comparison of Cp at the base of the models used in the study (top) and (below) the wake structure near the base visualised using the iso-surface of total $Cp = -0.2$ for **a** GB, **b** FB, **c** AB, **d** SB, **e** WB, and **f** HB

lower Cd_m values in GB and WB compared to the configurations SB and HB, where the highest mirror drag values are predicted, as shown in Table 2.

For all configurations examined, the flow separation from the mirror results in the formation of two distinct counter-rotating vortices, V_1 and V_2, originating from the top and bottom faces of the mirror, respectively as shown in Fig. 9. Although the changes in forebody configurations had a negligible impact on the generation of these mirror-induced vortices. However, it's worth highlighting that there are variations within the structures of V_1 and V_2 themselves, influenced by the specific forebody configuration. In all cases, both V_1 and V_2 strengthen as they progress towards the vehicle's wake, as detailed in Table 3, with V_1 being stronger than V_2. Importantly, this behaviour is not influenced by the variations in the forebody configuration. However, the angle at which these vortices traverse in relation to the mirror's central axis (α' and α) is asymmetrical in nature, and α' is influenced by the presence of the A-pillar, as shown in Fig. 9. For the SB configuration, α' is the most pronounced among those examined, due to the interaction of flow from the A-pillar with the horseshoe vortex around the mirror. Conversely, in cases such as WB, the A-pillar's angle aids in aligning V_1 and V_2 more closely with the mirror's central axis in the streamwise direction.

The effect of mirror-induced vortices on the vehicle's wake is depicted in Fig. 10, where flow separation is more prominent on the mirror side (CDw_m) than the no-mirror side (CDw'_m). The pressure imbalance between CDw_m and CDw'_m indicates that bodies with inherent sharp edges at the base, such as the GB, tend to experience less imbalance compared to those with rounded edges, as presented in the last column of Table 2. All the investigated squareback configurations exhibit the emergence of a toroidal vortex ring in the near wake of the body (Roumeas et al. 2009; Castro and Robins 1977). Flow separation from the roof, underbody, and side walls of the vehicle creates shear layers, which ultimately converge at the rear edges of the vehicle's base. These converging shear layers give
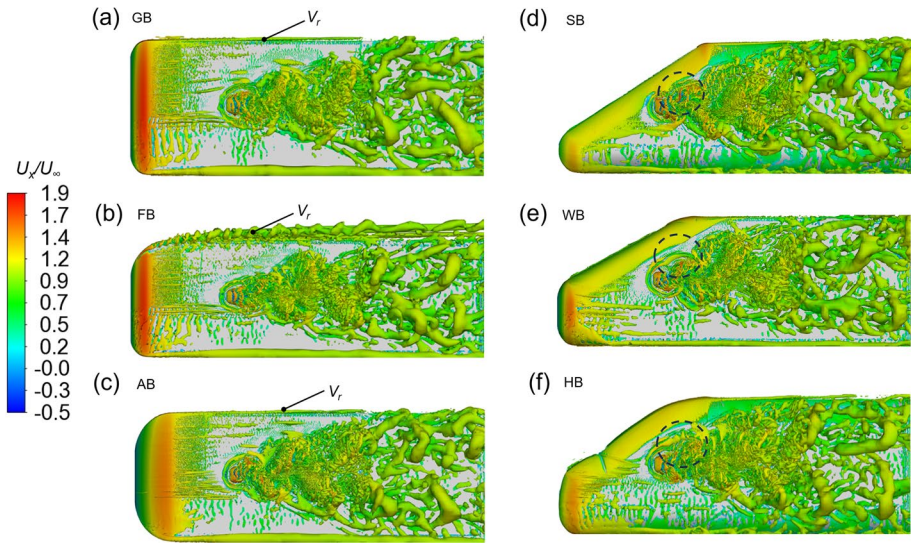
Fig. 11 Comparison of vortical structures of an instantaneous flow field visualized by iso-surface of $Q = 1000 \text{ s}^{-2}$ colored with instantaneous streamwise velocity for **a** GB, **b** FB, **c** AB, **d** SB, **e** WB, and **f** HB. Here V_r represents the vortex emanating from the leading edge of the roof and dotted circle indicating the location where the flow from the A-pillar is interacting with the flow around the side view mirror

rise to a circular vortex ring, a characteristic feature of squareback vehicle wakes. Conditions such as nearly equal strength of upper and lower horseshoe vortices in the separation bubble can lead to their merging and the subsequent development of such a ring vortex, as shown in Fig. 7. For configurations with sharp corners at the base, such as the GB, FB, WB, and AB, the toroidal vortex ring shows a high degree of similarity. In the case of bodies with curved corners on the base, such as SB and HB, it indicates a low-pressure region closer to the w_m side covering the curved corners. This indicates that the flow is more separated compared to the sharp-edged bodies, owing to the mirror-induced vortex (V_1) traversing along the rounded edges, as shown in Fig. 9, and evidenced by the larger angle α' associated with V_1 for both SB and HB.

To gain insight into the interaction of the A-pillar with the sideview mirror, the instantaneous flow structures for different forebody cases are compared, as shown in Fig. 11. At the upstream of the mirror, the presence of a horseshoe vortex is evident for all cases, with highly unsteady smaller eddies generated downstream that interact with the A-pillar vortices, particularly in the case of SB than compared to the WB and HB. Interestingly, for cases without the A-pillar, a distinct vortex roll-up of the roof vortex was observed in FB (See Fig. 11b, marked by V_r) from the leading edge of the roof which is less prominent with the other cases such as the GB and AB. This roll-up is due to the presence of a sharp edge connecting the front curvature of the body and roof, which is unique to this configuration. Examining the flow behaviour closer to the mirror and side window, the time-averaged wall shear stresses of the flow on the forebody proximal to the side-view mirror and the side window are assessed, as shown in Fig. 12. The flow characteristics around the side-view mirror can be characterised based on the characteristics length as presented in previous studies of the standard cube cases by Wang et al. (Ask and Davidson 2009; Wang et al. 2020). The wake of the mirror is indicated by L_{ws}, the smallest wake length is
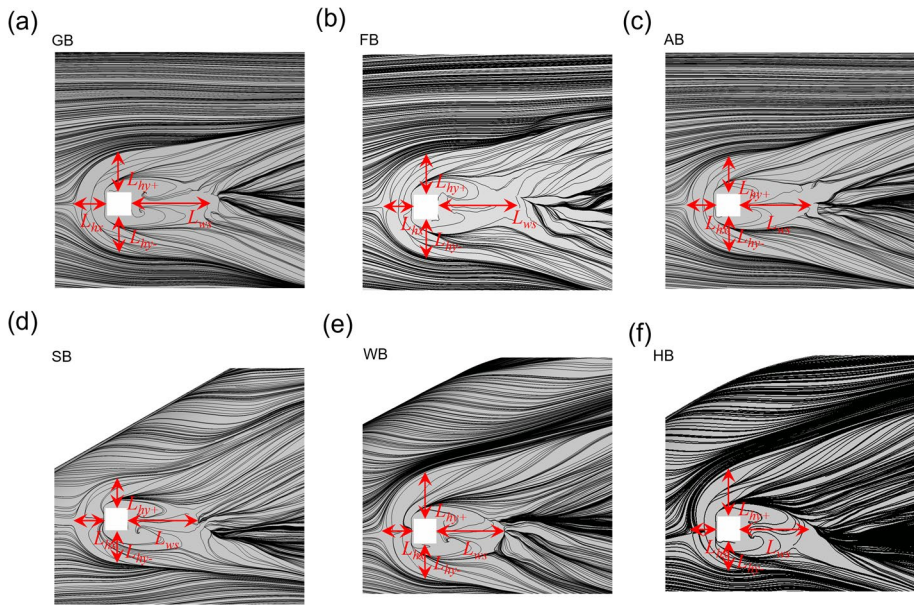
Fig. 12 Comparison of time-averaged wall shear stresses generated around side window and side-view mirror mounted on vehicle body for **a** GB, **b** FB, **c** AB, **d** SB, **e** WB, and **f** HB

Table 4 Comparison of the normalised lengths of time-averaged flow feature around the forebody between all the squareback models investigated in this study

Case	L_{hx}	L_{hy+}	L_{hy}	L_{ws}
GB	1.37	1.66	1.45	3.20
FB	1.35	1.72	1.49	3.19
AB	1.32	1.92	1.79	3.09
SB	1.35	1.12	1.72	3.17
WB	1.50	2.11	1.70	3.00
HB	1.30	2.06	1.28	3.06

observed for the WB for all the cases investigated, whereas for the no A-pillar configurations, the smallest wake is reported for the AB. It is observed that the horseshoe vortex that is formed around the mirror, is asymmetric in the normal direction for all cases examined. In most instances, L_{hy+} is dominant, as presented in Table 4, except in the case of SB, where L_{hy-} prevails due to the A-pillar's proximity to the side-view mirror. In the SB case, the flow emanating from the A-pillar interacts with the horseshoe vortex in the L_{hy+} direction, consequently pushing the horseshoe vortex downwards of the mirror, which is also evidenced in Fig. 11d.

Considering that the side-view mirror is the major source of noise generation in vehicles, the interaction of the flow from the mirror emanating from various forebody configurations with other surfaces causes noise generation on the side window, and eventually gets radiated from the vehicle. In the following section, the generation of this aerodynamic noise and its directivity patterns representing the angular distribution of the radiated sound field is discussed.
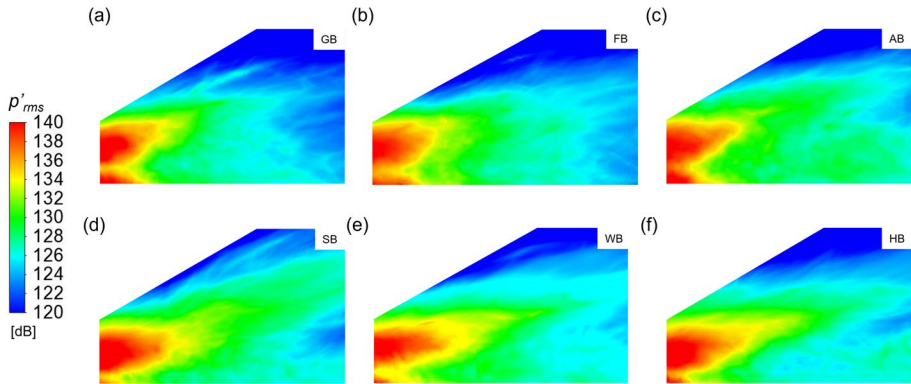
Fig. 13 Comparison of p'_{rms} on the side window between **a** GB, **b** FB, **c** AB, **d** SB, **e** WB, and **f** HB

4.2 Analysis of the Aerodynamic Noise Generated and Radiated

Figure 13 illustrates the overall distribution of hydrodynamic pressure fluctuations (p') on the side window, represented by the root-mean-square of (p'), given by p'_{rms}. The numerical predictions suggest that high-intensity pressure fluctuations affecting the side window are primarily located within the horseshoe vortex and L_{ws}. The intensity levels predicted for SB configuration are in agreement with the experimental data (Nusser 2019). Notably, the side window of the SB configuration experiences higher overall intensity levels, while the GB exhibits lower intensity levels. The high-intensity zones situated behind the side-view mirror exhibit asymmetrical behaviour, a result of the nature of the horseshoe vortex development, as indicated by the values presented for L_{hy+} and L_{hy-} in Table 4. In cases with A-pillars, the interaction of upstream flow with the horseshoe vortex is more pronounced, leading to pressure fluctuations extending up to the trailing edges of the side window. In contrast, for bodies without A-pillars, the pressure fluctuations diminish after the
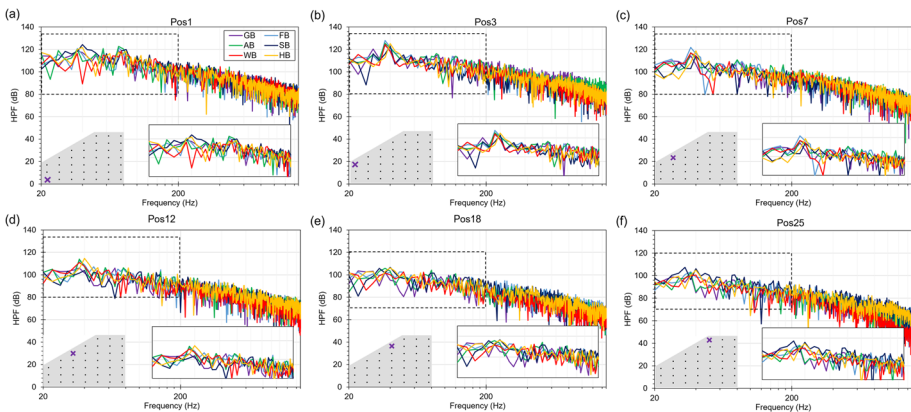

Fig. 14 Hydrodynamic pressure fluctuations extracted at **a** pos 1, **b** pos 3, **c** pos 7, **d** pos 12, **e** pos 18, and **f** pos 25 for all the bodies investigated. The location of each probe position is represented by 'x' in the schematic and the exact coordinates from the vehicles' origin are presented in the supplementary data

Table 5 Comparison of Overall Sound Pressure Level (OASPL) emanating from the different vehicle bodies investigated

Microphone Locations	GB (dB)	FB (dB)	AB (dB)	SB (dB)	WB (dB)	HB (dB)
M1 (1.6, 0.92, 0.9 m)	101.93	103.13	103.19	107.67	104.86	105.36
M2 (1.6, 0.92, 1.8 m)	75.30	78.11	77.20	76.18	76.85	75.20
M3 (1.6, 0.92, 3.6 m)	62.84	63.78	63.89	63.99	63.95	63.43

The microphone locations are given from the origin of the vehicle

midsection of the side window, as shown in Fig. 13. Hydrodynamic pressure fluctuations (HPF) extracted at positions 18 and 25, closer to the edges of the side window, indicate a reduction in intensity levels for bodies without A-pillars, as depicted in Fig. 14. Notably, experimental data reveals the presence of an aeolian tone at 40 Hz for SB (as shown in Fig. 6 at Pos1), while HB also reports peak intensity at 40 Hz. Conversely, other bodies display a slight shift in peak intensity by approximately ~3–4 Hz, consistent across locations where HPF is extracted (Pos 3, 7, 12, 18, and 25). This shift can be attributed to the presence of the A-pillar, which alters the horseshoe vortex and delays vortex shedding from the mirror, as illustrated in Fig. 11 using dotted ovals.

$$p'_{nrms} = \sqrt{\frac{1}{N} \sum_{n=1}^{N} \left(p'_n\right)^2}$$

$$OASPL = 10 \log_{10} \left(\frac{p'^2_{nrms}}{p^2_{ref}} \right) \tag{3}$$

where p'_n sound pressure fluctuation obtained at far-field microphone, p'_{nrms} represents the root mean square of the sound pressure fluctuations obtained at far-field microphone and p_{ref} indicate reference pressure ($p_{ref} = 2 \times 10^{-5}$ pa).

Based on the analysis of fluctuating pressure distributions derived from the SBES simulations discussed earlier, the FW-H method is employed to predict far-field noise at various receiver locations. The evaluation of noise propagation from the bodies are evaluated at distances of 0.9, 1.35, and 1.8 m in spanwise direction away from the vehicles' origin reveals that SB reports the highest overall sound pressure level (OASPL), while GB reports the lowest, as detailed in Table 5. In this study, the OASPL is defined the logarithmic ratio between root mean square of sound pressure fluctuations obtained at far-field microphone location (p_{nrms}ʹ) to the reference pressure (p_{ref}) which is taken as 2×10^{-5} pa, and mathematical from is shown in Eq. (3). The pattern of the radiated noise, obtained through a circular array of 36 microphones placed at three different locations, demonstrates that when measured in close proximity ($z = 0.9$ m) to all the key sources within the forebody of each vehicle configuration, including the side window, side-view mirror, frame, and, where applicable, the A-pillar, the pattern resembles a cardioid-like shape characterized by clearly defined lobes. The minimum point, at 270°, represents the direction of oncoming flow where the dB value is the lowest in this location. Notably, the SB predicts significantly higher dB values closer to 0–60°, indicating a strong asymmetry, perhaps influenced by the A-pillar. In contrast, the other models demonstrate symmetric trends, particularly the GB, which exhibits symmetric lobes but at reduced dB levels. This indicates a strong influence
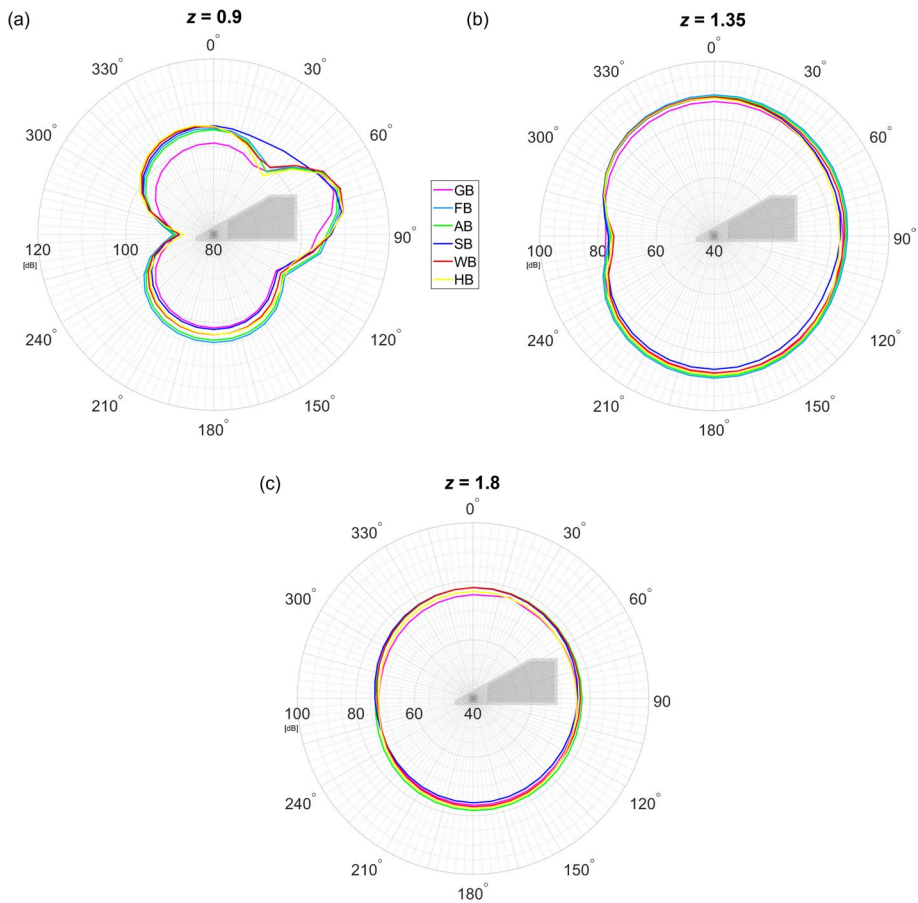
Fig. 15 Comparison of the structure of the noise radiated from the sources present on the forebody between all the cases investigated at **a** $z=0.9$ m, **b** $z=1.35$ m, and **c** $z=1.8$ m

of multiple high-intensity sources on the radiation pattern, demonstrated by the visible contribution of the A-pillar in SB, as depicted in Fig. 15a.

As the probing distance from the vehicle increases ($z=1.35$ m), the directivity pattern transitions into a sub-cardioid-like (Fig. 15b) structure where there is no clearly defined minimum point in this location, except for WB that still exhibits some features at 270°, where the dB value is at its minimum within this probed location. In contrast, GB shows the least evidence of the presence of a minimum point within the radiated sound pattern. At this stage, the radiated patterns from all cases become more oblique but tend to be symmetrical. The diminishing minimum point of sound radiated, and less pronounced lobes indicate a reduction in the directivity of noise sources. The symmetry of the sub-cardioid-like pattern at this stage suggests that the directional bias of noise generation decreases with distance. By $z=1.8$ m, all configurations tend to resemble a monopole-like pattern, indicating that no specific noise source dominates the radiation direction. GB consistently maintains lower dB levels compared to

the others, as seen in Fig. 15c. While the forebody configuration differences in bodies without A-pillars do not significantly alter the pattern of radiated noise, the transition from a cardioid-like to a sub-cardioid-like to eventually a monopole-like pattern illustrates the significant influence of specific forebody components on the radiated noise.

5 Conclusions

In this paper, the Stress-Blended Eddy Simulation (SBES), a Scale-Resolving Simulation, in conjunction with the Ffowcs Williams-Hawkings (FW-H) method, was employed to gain insights into the near-field flow and far-field noise characteristics of two distinct classes of standard vehicle configurations: those with A-pillars, namely the Generic Body (GB) and the Ahmed Body (AB), and those without A-pillars, namely the Windsor Body (WB) and the SAE-T4 Body (SB). To expand the scope of this work, two additional configurations were introduced, namely the Fused Body (FB) and the Hybrid Body (HB), by combining design features from bodies without A-pillars and those with A-pillars, whilst preserving consistent design parameters and features across all configurations. The numerical predictions have been rigorously validated and demonstrate good agreement with the available experimental data for the (SB) model, as reported by Nusser (2019), thus serving as a benchmark for the evaluation of our numerical predictions.

- One of the primary emphases of this study details the flow separation and the formation of mirror-induced vortices (V_1 and V_2) on the upper and lower regions of the mirror. The formation of these vortices, while relatively insensitive to variations in forebody design, significantly affects the overall vehicle wake. Notably, the vortices' angles of incidence (α' and α) are subject to the presence of A-pillars, revealing an interaction between the nature of the forebody design and mirror-induced vortices, affecting both the aerodynamics and aeroacoustics performance of the vehicle. It is noted that the sharp-edged base vehicle configurations exhibit similar toroidal vortex patterns, while vehicles with rounded base edges yield distinct wake behaviours due to the modulating influence of mirror-induced vortices. Overall, configurations lacking A-pillars consistently generate increased negative lift (downforce) in contrast to those with A-pillars. While a direct relationship remains elusive, an apparent trend emerges, suggesting a potential association between higher downforce and reduced radiated noise levels for both class of vehicle configurations.
- In configurations featuring A-pillars, a significant interaction, particularly for the SB model, occurs between the upstream flow and the horseshoe vortex, resulting in the extension of pressure fluctuations towards the trailing edges of the side window. Conversely, configurations without A-pillars display reduced pressure fluctuations beyond the midsection of the side window. The numerical predictions detect a 40 Hz aeolian tone in SB in agreement with experimental data and HB, while other configurations exhibit a ~ 3–4 Hz shift in peak intensity in (dB) at various locations probed. This shift can be ascribed to the A-pillars' impact on the horseshoe vortex, causing a delay in vortex shedding from the mirror.
- Investigating the radiated sound, closer to the vehicle, all models exhibit a cardioid-like pattern, which gradually transitions into a sub-cardioid-like shape before ultimately resembling a monopole-like pattern as the distance from the vehicle increases. However, the SB model demonstrates an intriguing asymmetry. While most models show

balanced dB levels between the two lobes indicating the 0° and the 180° directions, the SB model exhibits higher dB levels closer to 0° (towards the A-pillar direction) compared to the 180° side (towards the ground). This indicates that the SB model's noise source, likely influenced by the A-pillar and specific vehicle features, had a directional bias towards the front of the vehicle, resulting in a unique noise pattern. The outcome of this study revealed that the Generic Body (GB) consistently exhibited the lowest radiated OASPL levels at all probed locations, while the Squareback (SB) model exhibited the highest levels.

Despite the limited availability of the experimental data for validation for all configurations examined, the strong agreement with the validated SB model highlights the reliability of the numerical predictions in understanding the impact of forebody design on aerodynamics and aeroacoustics. However, by expanding the experimental comparisons for a broader set of forebody configurations can further enhance the scope of this study.

Author Contributions Both the authors contributed to the study conception and design. Material preparation, data collection and analysis were performed by HV and KKC. The first draft of the manuscript was written by both authors and commented on subsequent versions of the manuscript leading to the final manuscript. Both the authors read and approved the final manuscript.

Data Availability The data that support the findings of this study are available from the following link: Viswanathan, H., and Chode, K.K. (2023). Standard Squareback models for Aerodynamics and Aeroacoustics Research. SHU Research Data Archive (SHURDA). http://doi.org/https://doi.org/10.17032/shu-0000000183.

Declarations

Competing interests The authors declare no competing interests.

Conflict of interest The authors have no conflicts of interest to declare that are relevant to the content of this article.

Ethical Approval Not applicable.

Informed Consent Not applicable.

References

Ahmed, S.R., Ramm, G., Faltin, G.: Some salient features of the time-averaged ground vehicle wake. In: SAE Technical Paper Series. SAE International Congress and Exposition. SAE International (1984)

Ask, J., Davidson, L.: A numerical investigation of the flow past a generic side mirror and its impact on sound generation. J. Fluids Eng. (2009). https://doi.org/10.1115/1.3129122

Ask, J., Davidson, L.: Flow and dipole source evaluation of a generic SUV. J. Fluids Eng. (2010). https://doi.org/10.1115/1.4001340

Beck, A., Munz, C.D.: Direct aeroacoustic simulations based on high order discontinuous Galerkin schemes. In: Computational acoustics, vol. 579, pp. 159–204. Springer, Cham (2018)

Braun, M.E., Walsh, S.J., Horner, J.L., Chuter, R.: Noise source characteristics in the ISO 362 vehicle pass-by noise test: literature review. Appl. Acoust. **74**, 1241–1265 (2013). https://doi.org/10.1016/j.apacoust.2013.04.005

Camussi, R., Bennett, G.J.: Aeroacoustics research in Europe: the CEAS-ASC report on 2019 highlights. J. Sound Vib. **484**, 115540 (2020). https://doi.org/10.1016/j.jsv.2020.115540

Castro, I.P., Robins, A.G.: The flow around a surface-mounted cube in uniform and turbulent streams. J. Fluid Mech. **79**, 307–335 (1977)

Chode, K.K., Viswanathan, H., Chow, K.: Numerical investigation on the salient features of flow over standard notchback configurations using scale resolving simulations. Comput. Fluids **201**, 104666 (2020). https://doi.org/10.1016/j.compfluid.2020.104666

Chode, K.K., Viswanathan, H., Chow, K.: Noise emitted from a generic side-view mirror with different aspect ratios and inclinations. Phys. Fluids **33**, 084105 (2021). https://doi.org/10.1063/5.0057166

Chode, K.K., Viswanathan, H., Chow, K., Reese, H.: Investigating the aerodynamic drag and noise characteristics of a standard squareback vehicle with inclined side-view mirror configurations using a hybrid computational aeroacoustics (CAA) approach. Phys. Fluids (2023). https://doi.org/10.1063/5.0156111

Dawi, A.H., Akkermans, R.A.: Spurious noise in direct noise computation with a finite volume method for automotive applications. Int. J. Heat Fluid Flow **72**, 243–256 (2018)

Dawi, A.H., Akkermans, R.A.D.: Direct noise computation of a generic vehicle model using a finite volume method. Comput. Fluids **191**, 104243 (2019). https://doi.org/10.1016/j.compfluid.2019.104243

Duell, E.G., George, A.R.: Experimental study of a ground vehicle body unsteady near wake. In: SAE Technical Paper Series. International Congress & Exposition. SAE International (1999)

Egorov, Y., Menter, F.R., Lechner, R., Cokljat, D.: The scale-adaptive simulation method for unsteady turbulent flow predictions. Part 2: application to complex flows. Flow Turbul. Combust. **85**, 139–165 (2010). https://doi.org/10.1007/s10494-010-9265-4

Ekman, P., Wieser, D., Virdung, T., Karlsson, M.: Assessment of hybrid RANS-LES methods for accurate automotive aerodynamic simulations. J. Wind Eng. Ind. Aerodyn. **206**, 104301 (2019). https://doi.org/10.1016/j.jweia.2020.104301

Evans, D., Hartmann, M., Delfs, J.: Beamforming for point force surface sources in numerical data. J. Sound Vib. **458**, 303–319 (2019). https://doi.org/10.1016/j.jsv.2019.05.030

Fares, E.: Unsteady flow simulation of the Ahmed reference body using a lattice Boltzmann approach. Comput. Fluids **35**, 940–950 (2006)

Frank, H.M., Munz, C.D.: Large eddy simulation of tonal noise at a side-view mirror using a high order discontinuous Galerkin method. In: 22nd AIAA/CEAS Aeroacoustics Conference. American Institute of Aeronautics and Astronautics (2016)

Frank, H.M., Munz, C.-D.: Direct aeroacoustic simulation of acoustic feedback phenomena on a side-view mirror. J. Sound Vib. **371**, 132–149 (2016a). https://doi.org/10.1016/j.jsv.2016.02.014

Ganuga, R.S., Viswanathan, H., Sonar, S., Awasthi, A.: Fluid-structure interaction modelling of internal structures in a sloshing tank subjected to resonance. Int. J. Fluid Mech. Res. **41**, 145–168 (2014). https://doi.org/10.1615/interjfluidmechres.v41.i2.40

Goetchius, G.: Leading the charge—the future of electric vehicle noise control. Sound Vib. **45**, 5–8 (2011)

Guilmineau, E., Deng, G., Leroyer, A., Queutey, P., Visonneau, M., Wackers, J.: Assessment of hybrid RANS-LES formulations for flow simulation around the Ahmed body. Comput. Fluids **176**, 302–319 (2018)

Hamiga, W.M., Ciesielka, W.B.: Aeroaocustic numerical analysis of the vehicle model. Appl. Sci. **10**, 9066 (2020). https://doi.org/10.3390/app10249066

Hartmann, M., Ocker, J., Lemke, T., Mutzke, A., Schwarz, V., Tokuno, H., Toppinga, R., Unterlechner, P., Wickern, G.: Wind Noise Caused by the Side-Mirror and A-Pillar of a Generic Vehicle Model. In 18th AIAA/CEAS Aeroacoustics Conference (33rd AIAA Aeroacoustics Conference). American Institute of Aeronautics and Astronautics (2012)

He, Y., Schröder, S., Shi, Z., Blumrich, R., Yang, Z., Wiedemann, J.: Wind noise source filtering and transmission study through a side glass of DrivAer model. Applied Acoust. **160**, 107161 (2020). https://doi.org/10.1016/j.apacoust.2019.107161

He, Y., Wan, R., Liu, Y., Wen, S., Yang, Z.: Transmission characteristics and mechanism study of hydrodynamic and acoustic pressure through a side window of DrivAer model based on modal analytical approach. J. Sound Vib. **501**, 116058 (2021a)

He, Y., Wen, S., Liu, Y., Yang, Z.: Wind noise source characterization and transmission study through a side glass of DrivAer model based on a hybrid DES/APE method. Proc. Inst. Mech. Eng. Part D J. Automob. Eng. **235**, 1757–1766 (2021b)

Helfer, M.: General aspects of vehicle aeroacoustics. In: Proceedings of the Lecture Series on Road Vehicle Aerodynamics, Sint-Genesius-Rode, Belgium, 30 May–3 June 2005 (2005)

Hesse, F., Morgans, A.S.: Characterization of the unsteady wake aerodynamics for an industry relevant road vehicle geometry using LES. In: Flow, Turbulence and Combustion, vol. 110, pp. 855–887. Springer Science and Business Media LLC (2023)

Höld, R., Brenneis, A., Eberle, A., Schwarz, V., & Siegert, R.: Numerical simulation of aeroacoustic sound generated by generic bodies placed on a plate. I - Prediction of aeroacoustic sources. In: 5th AIAA/CEAS Aeroacoustics Conference and Exhibit. 5th AIAA/CEAS Aeroacoustics Conference and Exhibit. American Institute of Aeronautics and Astronautics (1999)

Howard, R.J.A., Pourquie, M.: Large eddy simulation of an Ahmed reference model. J. Turbul. (2002). https://doi.org/10.1088/1468-5248/3/1/012

Jadon, V., Agawane, G., Baghel, A., Balide, V., Banerjee, R., Getta, A., Viswanathan, H., Awasthi, A.: An experimental and multiphysics based numerical study to predict automotive fuel tank sloshing noise. In: SAE Technical Paper Series. SAE 2014 World Congress & Exhibition. SAE International (2014)

Kabat Vel Job, A., Sesterhenn, J.: Prediction of the interior noise level for automotive applications based on time-domain methods. In: INTER-NOISE and NOISE-CON Congress and Conference Proceedings, vol. 253, pp. 6000–6010. Institute of Noise Control Engineering. https://www.ingentaconnect.com/content/ince/incecp/2016/00000253/00000002/art00019 (2016)

Kapellos, C.S., Papoutsis-Kiachagias, E.M., Giannakoglou, K.C., Hartmann, M.: The unsteady continuous adjoint method for minimizing flow-induced sound radiation. J. Comput. Phys. **392**, 368–384 (2019). https://doi.org/10.1016/j.jcp.2019.04.056

Krajnovic, S., Davidson, L.: Numerical study of the flow around a bus-shaped body. J. Fluids Eng. **125**, 500–509 (2003). https://doi.org/10.1115/1.1567305

Menter, F.: Stress-blended eddy simulation (SBES)—A new paradigm in hybrid RANS-LES modelling. In: Progress in Hybrid RANS-LES Modelling, Notes on Numerical Fluid Mechanics and Multidisciplinary Design, vol. 137, pp. 27–37. Springer (2018)

Menter, F., Hüppe, A., Matyushenko, A., Kolmogorov, D.: An overview of hybrid rans–LES models developed for industrial CFD. Appl. Sci. **11**, 2459 (2021). https://doi.org/10.3390/app11062459

Menter, F.R., Hüppe, A., Flad, D., Garbaruk, A.V., Matyushenko, A.A., Stabnikov, A.S.: Large Eddy simulations for the Ahmed car at 25° slant angle at different Reynolds numbers. In: Flow Turbulence and Combustion. Springer Science and Business Media LLC (2023)

Müller, S., Becker, S., Gabriel, C., Lerch, R., Ullrich, F.: Flow-induced input of sound to the interior of a simplified car model depending on various setup parameters. In: 19th AIAA/CEAS Aeroacoustics Conference. 19th AIAA/CEAS Aeroacoustics Conference. American Institute of Aeronautics and Astronautics (2013)

Nusser, K., Becker, S.: Numerical investigation of the fluid structure acoustics interaction on a simplified car model. Acta Acust. **5**, 22 (2021). https://doi.org/10.1051/aacus/2021014

Nusser, K., Müller, S., Scheit, C., Oswald, M., Becker, S.: Large Eddy simulation of the flow around a simplified car model. In: Direct and Large-Eddy Simulation X, pp. 243–249. Springer International Publishing (2017)

Nusser, K.: Investigation of the Fluid-Structure-Acoustics Interaction on a Simplified Car Model. Ph.D. Thesis, Friedrich-Alexander University Erlangen-Nürnberg (2019)

Oettle, N., Sims-Williams, D.: Automotive aeroacoustics: an overview. Proc. Inst. Mech. Eng. Part D J. Automob. Eng. **231**, 1177–1189 (2017). https://doi.org/10.1177/0954407017695147

Page, G.J., Walle, A.: Towards a standardized assessment of automotive aerodynamic CFD prediction capability—AutoCFD 2: Windsor Body Test Case Summary. In: SAE Technical Paper Series. WCX SAE World Congress Experience. SAE International (2022)

Perry, A.-K., Pavia, G., Passmore, M.: Influence of short rear end tapers on the wake of a simplified square-back vehicle: wake topology and rear drag. Exp. Fluids (2016a). https://doi.org/10.1007/s00348-016-2260-3

Perry, A.-K., Almond, M., Passmore, M., Littlewood, R.: The study of a bi-stable wake region of a generic squareback vehicle using tomographic PIV. SAE Int. J. Passenger Cars Mech. Syst. **9**, 743–753 (2016b). https://doi.org/10.4271/2016-01-1610

Read, C., Viswanathan, H.: An aerodynamic assessment of vehicle-side wall interaction using numerical simulations. Int. J. Autom. Mech. Eng. **17**, 7587–7598 (2020). https://doi.org/10.15282/ijame.17.1.2020.08.0563

Roumeas, M., Gillieron, P., Kourta, A.: Analysis and control of the near-wake flow over a square-back geometry. Comput. Fluids **38**, 60–70 (2009)

Su, X., He, K., Xu, K., Gao, G., Krajnović, S.: Comparison of flow characteristics behind squareback bluff-bodies with and without wheels. Phys. Fluids **35**, 035114 (2023). https://doi.org/10.1063/5.0138305

Viswanathan, H.: Aerodynamic performance of several passive vortex generator configurations on an Ahmed body subjected to yaw angles. J. Braz. Soc. Mech. Sci. Eng. (2021). https://doi.org/10.1007/s40430-021-02850-8

Viswanathan, H., Chode, K.K.: The influence of forebody topology on aerodynamic drag and aeroacoustics characteristics of Squareback Vehicles using CAA. In: Aerovehicles 5, Poiters, France, 12–14 June 2023. Available from: https://shura.shu.ac.uk/id/eprint/32049 (2023)

Wagner, C., Hüttl, T., Sagaut, P. (eds.): Large-Eddy Simulation for Acoustics. Cambridge University Press (2007)

Wang, Y., Thompson, D., Hu, Z.: Numerical investigations on the flow over cuboids with different aspect ratios and the emitted noise. Phys. Fluids **32**, 025103 (2020)

Wang, D., Sun, M., Shen, X., Chen, A.: Aerodynamic characteristics and structural behavior of sound barrier under vehicle-induced flow for five typical vehicles. J. Fluids Struct. **117**, 103816 (2023). https://doi.org/10.1016/j.jfluidstructs.2022.103816

Windsor, S.: The effect of rear end shape an road vehicle aerodynamic drag. C427/6/031, IMechE Autotech, UK (1991)

Publisher's Note Springer Nature remains neutral with regard to jurisdictional claims in published maps and institutional affiliations.